Plasma Physics and Controlled Fusion

Gyrokinetic simulations of core turbulence and thermal transport in the high-β_P discharge on EAST

To cite this article: Y C Hu *et al* 2023 *Plasma Phys. Control. Fusion* **65** 055023

OPEN ACCESS
IOP Publishing

Plasma Physics and Controlled Fusion

Plasma Phys. Control. Fusion **65** (2023) 055023 (10pp)

https://doi.org/10.1088/1361-6587/acc482

Gyrokinetic simulations of core turbulence and thermal transport in the high-β_{P} discharge on EAST

Y C Hu[1,2], **L Ye**[1,*], **X Z Gong**[1,*], **A M Garofalo**[3], **J P Qian**[1], **J Huang**[1], **B Zhang**[1], **P F Zhao**[1,2], **Y J Hu**[1], **Q L Ren**[1], **J Y Zhang**[1,2], **X X Zhang**[1,2], **R R Liang**[1,2] and **Z H Wang**[1,2]

[1] Institute of Plasma Physics, Hefei Institutes of Physical Science, Chinese Academy of Sciences, Hefei 230031, People's Republic of China
[2] University of Science and Technology of China, Hefei 230026, People's Republic of China
[3] General Atomics, PO Box 85608, San Diego, CA 92186-5608, United States of America

E-mail: lye@ipp.ac.cn and xz_gong@ipp.ac.cn

Received 9 October 2022, revised 6 February 2023
Accepted for publication 15 March 2023
Published 11 April 2023

Abstract

The properties of core turbulence and thermal transport are investigated for EAST high-β_{P} ($\beta_{\mathrm{P}} \sim 3.1$) plasmas with dominant electron heating ($T_{\mathrm{e}}/T_{\mathrm{i}} > 1$) via gyrokinetic simulation with the NLT code. Linear simulations identify that the electrostatic η_e-driven trapped electron mode (η_e-TEM) dominates in the core region ($\rho < 0.7$) and the ion temperature gradient (ITG) mode dominates in the out region ($\rho \geqslant 0.7$), consistent with the linear threshold analysis of micro-instabilities. Sensitivity analysis shows that the normalized electron density gradient (R/L_{ne}) and ITG (R/L_{Ti}) are two effective parameters to stabilize TEM instability. Nonlinear simulations are also carried out and compared with the experimental results, which show that the electron thermal internal transport barrier (ITB) in EAST high-β_{P} plasma is determined by the TEM-induced turbulence. A higher zonal flow shearing rate is observed in the ITB region ($0.2 < \rho < 0.34$), which can regulate energy transport induced by TEM turbulence and facilitate the formation of e-ITB. A plausible positive feedback mechanism to mitigate turbulence transport and improve energy confinement via enhanced ion heating is proposed for future experiments.

Keywords: high poloidal beta, gyrokinetic simulation, turbulence transport, trapped electron mode

(Some figures may appear in colour only in the online journal)

1. Introduction

High poloidal beta (β_{P}) plasma is desirable for steady-state operation, which is considered by the future international thermonuclear experimental reactor (ITER) tokamak [1]. In this scenario, the bootstrap effect self-generates a large proportion of the plasma current leading to less demand of the auxiliary current driving power. Here, $\beta_{\mathrm{P}} = P/\left(B_{\mathrm{P}}^2/2\mu_0\right)$, where P is the plasma thermal pressure and B_{P} is the poloidal magnetic field strength. In addition, a high β_{P} is associated with a high safety factor (q) in the edge, which is of benefit to avoid the plasma disruption [2]. The energy and particle confinement of the thermal plasma is a critical concern for high-β_{P} experiments since the bootstrapped current is proportional to the pressure gradient. It has long been recognized that a

---

[*] Authors to whom any correspondence should be addressed.

large value of the Shafranov shift, which is proportional to β_P, plays a pivotal role in the suppression of turbulence and related transport [3, 4].

The applicability of the high-β_P ($\beta_P \sim 4.7$) modes with $T_i \sim 45$ keV and high bootstrap fraction ($f_{BS} \sim 80\%$) has been exhibited on JT-60U [5]. JET has also obtained high energy confinement with $\beta_P \sim 2.0$ and a significant proportion of the bootstrap current ($I_{BS}/I_P \sim 0.7$) [6]. In recent high-β_P ($\beta_P \sim 2.0$) experiments on the DIII-D tokamak with dominant ion heating, it has been demonstrated that turbulence transport can be suppressed by the combination of reversed magnetic shear and Shafranov shift, so that strong internal transport barriers (ITBs) can be formed at a large radius far from the magnetic axis [7–9]. The dominant micro-turbulence instabilities in the D-IIID lower q_{95} high-β_P plasmas have been thoroughly investigated via gyrokinetic simulations with the GYRO code [10]. It was found that different types of drift-wave-like instabilities dominate in different radial regions. Specifically, the collisionless trapped electron mode (CTEM) dominates in the core region, while both the CTEM and electron temperature gradient (ETG) mode coexist in the ITB peak gradient region. Moreover, the ion temperature gradient (ITG) mode and ETG are dominant micro-instabilities at the ITB foot.

Most of the previous high-β_P experiments have been carried out under $T_i > T_e$ conditions and rely on a negative magnetic shear configuration to improve confinement. However, in a fusion reactor such as ITER, $T_e > T_i$ is expected over a large radial region in the center of the plasma due to the dominant electron heating provided by fusion α-particles, thus extending the high-β_P scenario in today's tokamaks with dominant electron heating and the conditions of $T_e > T_i$ are greatly necessary. Recently, significant progress of the high-confinement ($H_{98y2} \sim 1.3$) and high-β_P ($\beta_P \sim 2.0$) scenario has been made in the EAST 2021 campaign [11] with strong radio frequency (RF) heating, a monotonic q-profile and low-torque injection [12]. Preliminary transport analysis [12] indicates that the energy transport level is much higher than the neoclassical transport level, even though an electron thermal ITB can be formed inside the middle radius. Therefore, it is of significant importance to further investigate the properties of dominant turbulence and thermal transport in the existing EAST high-β_P scenario and to try to find a possible pathway to improve energy confinement by turbulence suppression for future experiments.

In this work, the properties of turbulence and turbulent transport in EAST core plasma are systematically investigated for the latest high-β_P scenario by gyrokinetic simulation with the NLT code [13]. The EAST discharge (#101473) studied here employs a high heating power combined with both RF and neutral beam injection (NBI), which can effectively elevate the β_P value in comparison with the previous experiments [12, 14, 15] using exclusive RF heating.

The remainder of this paper is organized as follows. A description of the experimental progress of high-β_P discharges on EAST as well as the physical model and simulation settings are presented in section 2. In section 3, the properties of turbulence and critical gradient threshold analysis are discussed. In section 4, nonlinear turbulence simulation and thermal transport analysis are presented. The conclusions are presented in section 5.

2. Experimental and simulation settings

In the 2021 EAST campaign, the high-β_P plasma ($\beta_P \sim 3.1$) has been obtained with about a total of 8.1 MW auxiliary on-axis heating power, including 2.6 MW NBI heating, 2.5 MW lower hybrid wave (LHW), 1.5 MW electron cyclotron heating (ECH) and 1.5 MW ion cyclotron resonance heating (ICRH). The main plasma parameters for the discharge #101473 are shown in figure 1: the plasma current $I_P = 0.4$ MA; the loop voltage is well controlled to be zero during the plasma flat-top, which indicates the fully non-inductive current drive conditions; the line-averaged electron density $n_e \sim 4.1 \times 10^{19}$ m^{-3}; $\beta_P \sim 3.1$ and $H_{98y2} \sim 1.2$.

In this work, the time slice $t = 4.5$ s is selected for transport analysis, where all of the auxiliary heating power is injected and the main plasma parameters, e.g. plasma current, density and poloidal beta, are relatively stable. The reconstructed equilibrium is obtained by EFIT [16], and the experimental plasma profiles are provided by the following diagnostics: the electron temperature (T_e) is measured by Thomson scattering (TS) diagnostics, the ion temperature (T_i) is measured by charge-exchange recombination spectroscopy and a tangential x-ray crystal spectrometer and the electron density (n_e) is reconstructed by a polarimeter-interferometer (POINT) [17] and reflectometers. The safety factor (q) profile on EAST is obtained using the method developed in [18], which is constrained by motional Stark-effect diagnostics. All the profiles are plotted in figure 2 in addition to the equilibrium configuration. It can be seen that the on-axis temperature of electrons $T_{e0} = 4.48$ keV is much higher than that of ions $T_{i0} = 1.35$ keV, which is induced by the strong electron heating power from the RF and NB. Therefore, the thermal transport of electrons not only determines the T_e profile but also has a significant impact on the T_i profile through energy transfer between electrons and ions, which is proportional to the temperature difference ($T_e - T_i$). The density profile is relatively flat in comparison with that of T_e, and the q-profile is monotonic with an edge safety factor $q_{95} \sim 8$.

The thermal diffusivities of electrons and ions are calculated from power balance analysis for the energy transport assessment. As shown in figure 3, the electron thermal diffusivity χ_e drops steeply from the outer region toward the core region in the area of $0.1 < \rho < 0.5$. This illustrates the formation of electron ITB (e-ITB) in the core region. Moreover, the ion thermal diffusivity is much higher than the neoclassical prediction, which implies the non-negligible role of the anomalous transport induced by micro-turbulence.

In this work, the NLT code is employed to investigate turbulence properties and thermal transport in the EAST high-β_P experiment. The NLT is a global δf gyrokinetic code [13] based on the I-transform theory [19–21], which

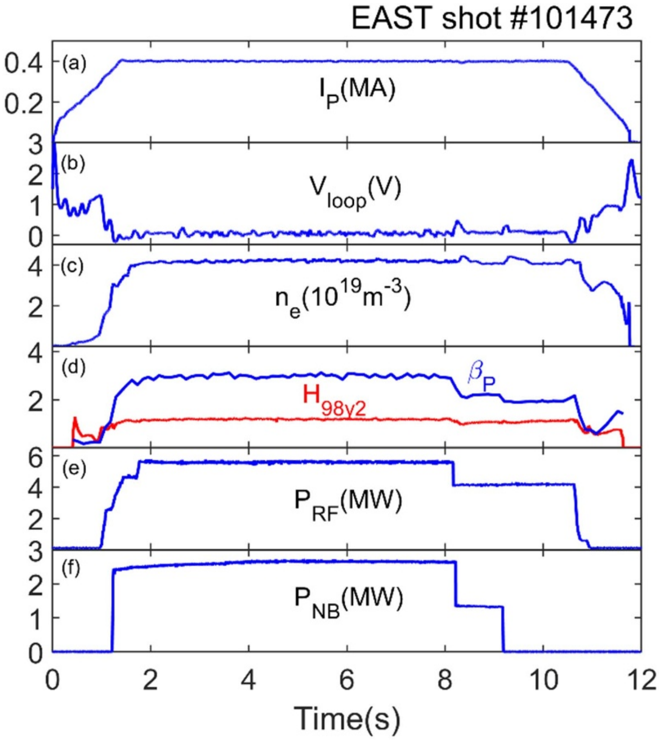

Figure 1. Time evolution of plasma parameters for high-β_P shot #101473 on EAST: (a) plasma current, (b) loop voltage, (c) line-averaged electron density, (d) poloidal beta β_P and the energy confinement enhanced factor H_{98y2}, (e) auxiliary heating powers of RF waves, including LHW, ICRH and ECH, (f) auxiliary heating powers of NBI.

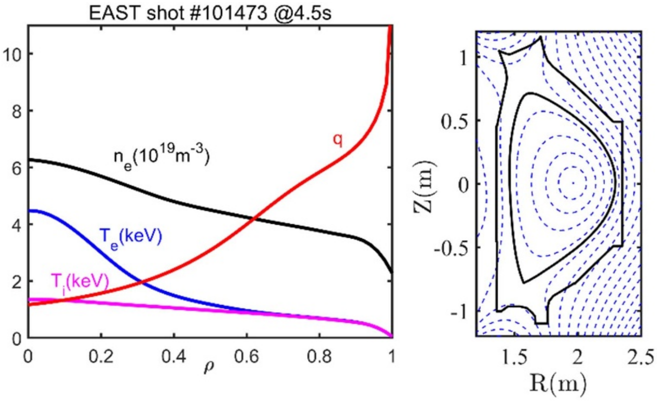

Figure 2. Profiles of T_e, T_i, n_e and q at $t = 4.5$ s for EAST discharge #101473 and the magnetic equilibrium configuration.

solves the coupled gyrokinetic Vlasov equation and the quasi-neutrality equation. The complete effects of drift kinetic electrons (for both passing and trapped electrons) are included in the NLT using the time-diffusion scheme [22] to mitigate the numerical instabilities induced by the high-frequency electrostatic Alfvén waves. The NLT has been successfully benchmarked for both linear and nonlinear simulations of electrostatic ITG–trapped electron mode (ITG–TEM) turbulence in tokamaks [22].

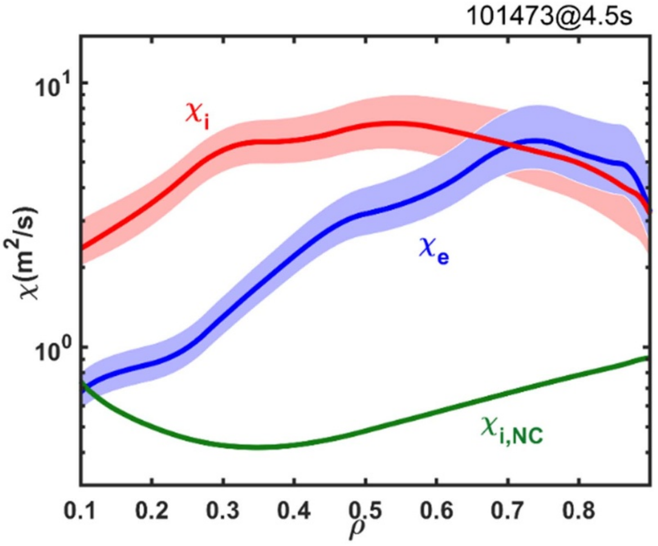

Figure 3. Thermal diffusivities of electrons (blue) and ions (red), and neoclassical diffusivity for the ions (green).

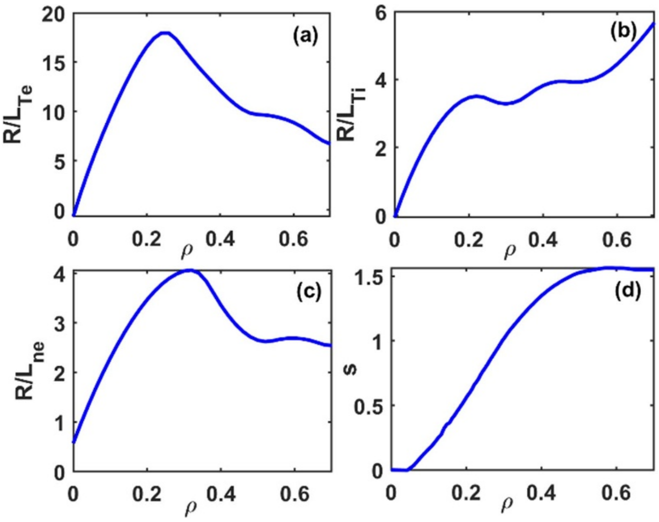

Figure 4. The scale length of (a) electron temperature, (b) ion temperature, (c) density and (d) magnetic shear of shot #101473.

It is generally acknowledged that drift-wave turbulence is mainly driven by the gradients of plasma temperature/density. To investigate the micro-instabilities and turbulence transport in EAST experiments, the normalized gradients for plasma profiles are calculated and shown in figure 4 for the time slice $t = 4.5$ s. It can be seen that the normalized gradient of electron temperature, R/L_{Te}, is much larger than that of the ion temperature R/L_{Ti} and electron density R/L_{ne}, which is consistent with the relatively small χ_e in the core region. The largest value for R/L_{Te} is 17.96 at $\rho = 0.25$, where $R/L_{\mathrm{Ti}} = 3.43$, $R/L_{\mathrm{ne}} = 3.84$ and the magnetic shear $s = 0.79$, respectively. This radial position $\rho = 0.25$ is therefore selected for the turbulence simulation and transport analysis. In addition, another radial position, $\rho = 0.5$, at the ITB foot is also selected for analysis.

The main simulation parameters are given as follows. The major radius $R_0 = 1.88$ m and the minor radius $a = 0.42$ m.

The toroidal magnetic field $B_0 = 2.26$ T. Three particle species are included in the simulation: the main ions (deuterium, D), impurity ions (the carbon impurities C^{+6}) and electrons, for which a realistic mass ratio $m_D/m_e = 3672$ is applied in the simulation. The density profile of carbon is calculated from the electron density profile and effective charge number, which are measured by POINT and visible bremsstrahlung [23], respectively. The temperature profile of carbon is assumed to be the same as that of the main ions. The numbers of computational grids are $n_x = 256$, $n_z = 16$, $n_{v\parallel} = 64$ and $n_\mu = 16$ for linear simulations. Here, (x, y, z) are field-aligned coordinates, which indicate radial, binormal and parallel directions, respectively. Here, $v_\parallel$ and μ are the parallel velocity and magnetic moment. The simulation time step $\delta_t = 0.012R_0/c_s$, where $c_s = \sqrt{T_e/m_i}$ is the ion acoustic velocity.

3. Linear gyrokinetic simulation results

3.1. Linear properties of micro-instabilities in the core region

To identify which instability dominates plasma energy transport in the ITB region, linear gyrokinetic simulations are carried out using the NLT code for this high-β_p discharge. The real frequency and growth rate for the unstable modes at $\rho = 0.25$ and $\rho = 0.5$ are plotted in figure 5 with $0.1 < k_\theta \rho_s < 1.5$. Here, $k_\theta = nq/r$ is the poloidal wave number, where n is the toroidal mode number. Meanwhile,$\rho_s = c_s/\Omega_s$ is the ion-sound Larmor radius, where $\Omega_s = eB/m_i$ is the gyro-frequency of ions. As seen in figure 5, the real frequency of the unstable mode increases monotonically with k_θ; and the frequency is a positive value for $k_\theta \rho_s < 2.5$, which indicates that the mode propagates in the electron diamagnetic direction in the NLT convention. Based on these observations, the dominant low-k ($k_\theta \rho_e \ll 1$) turbulence could be identified as the TEM. The growth rate for the unstable modes at $\rho = 0.25$ is obviously greater than that at $\rho = 0.5$, and thus we primarily analyze the most unstable mode in the core region where the profile gradient of T_e is the greatest.

A set of parameter scans are carried out to further investigate the properties of the micro-instabilities in the EAST high-β_P plasmas and to explore the potential mechanism to suppress core turbulence. Figure 6 depicts the parameter dependence of the linear growth rate and frequency of the unstable mode ($k_\theta \rho_s = 0.93$) on the normalized gradients and the temperature ratio, respectively. The temperature ratio impacts are shown in figure 6(a); it can be seen that as the electron-to-ion temperature ratio, $\tau = T_e/T_i$, decreases, the mode can be slightly destabilized. For $\tau > 1$, which is the typical value in a fusion reactor, the growth rate at $\tau = 1.2$ is 13% higher than that of the experimental value.

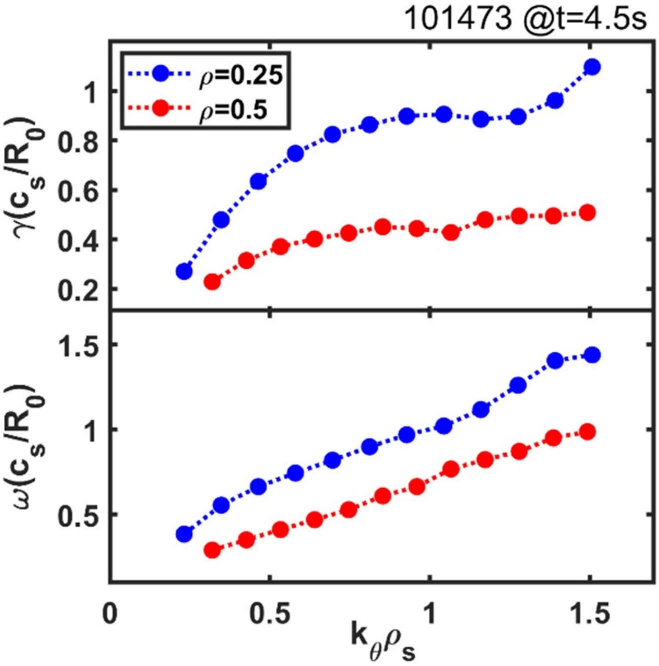

Figure 5. The linear growth rate and frequency of low-k mode instability against the normalized poloidal wave number in the peak gradient region (blue) and at the ITB foot (red) for EAST discharge #101473.

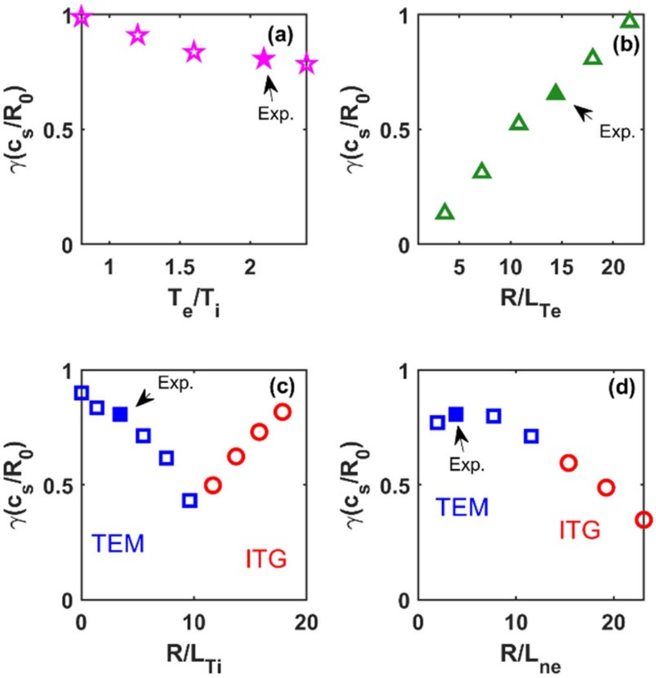

Figure 6. The dependence of growth rate on T_e/T_i (a), R/L_{Te} (b), R/L_{Ti} (c) and R/L_{ne} (d) from NLT. The blue squares indicate TEM mode, the red circles indicate ITG mode and the arrows correspond to experimental values.

In figure 6(b), as R/L_{Te} increases the growth rate of the TEM increases accordingly, which indicates the destabilization effect of the ETG on this micro-instability. Meanwhile, figure 6(d) shows that the mode can be stabilized by increasing R/L_{ne}. One can therefore confirm from these numerical results that the instability found here is the ETG-driven TEM (or η_e-TEM with $\eta_e = L_{ne}/L_{Te}$) [24, 25] instead of the density-gradient-driven TEM. The growth rate can only be slightly reduced by decreasing R/L_{ne} and a substantial growth rate (about 88% of that of the experimental value) persists, even with $R/L_{ne} = 0$. It is also interesting to note that as R/L_{ne} increases, the real frequency changes from a positive value to negative (ion diamagnetic direction), indicating a transition from the TEM to ITG mode. The density gradient also has a stabilization effect on the ITG mode as R/L_{ne} increases further, suggesting that the ITG mode observed here is η_i-ITG-like mode $(\eta_i = L_{ne}/L_{Ti})$ [26]. However, the stabilization effect induced by R/L_{ne} should be much stronger for the TEM than that for the ITG, so that the transition of the dominant instability appears as R/L_{ne} exceeds a critical value. Nevertheless, the simulation results indicate that the turbulence transport could be mitigated by peaked density profiles, which is consistent with previous predictions [27].

The dependence of the mode growth rate on the ITG is shown in figure 6(c). First, it is clear that the increased value of R/L_{Ti} can effectively suppress the TEM mode. Second, as R/L_{Ti} exceeds a critical value of $R/L_{\mathrm{Ti}} = 11$ (about three times that of the experimental value), the real frequency of the unstable mode is converted again into the ion diamagnetic direction, which implies the destabilization of the ITG mode by the ITG. The strongest suppression effects are observed near the critical point, where the growth rate can be reduced by about 50% compared with the nominal value. Above the critical value, the growth rate increases together with R/L_{Ti} monotonically. It has been pointed out in [28, 29] that when R/L_{Ti} is small, the TEM will become destabilized due to the non-adiabatic ion response (NAIR) term from the typical TEM dispersion relation reducing the magnitude of the adiabatic ion response. Conversely, when R/L_{Ti} increases gradually, the electron magnetic drift resonance, which destabilizes the TEM, is suppressed by the ion dynamics so that the TEM will be stabilized due to the NAIR, which has its sign changed as R/L_{Ti} increases.

The parameter dependence analysis of the linear growth rate above shows that the turbulence transport in EAST high-β_{P} plasmas can be effectively mitigated by core fueling with pellet injection to enhance the density gradient or by improving ion heating to enhance the ITG. However, a flat density profile in the core region is foreseen in fusion reactors (such as ITER or demonstration fusion power reactor (DEMO) with a large minor-radius value, while a peaked ion temperature profile is more relevant for fusion. Therefore, a plausible positive feedback mechanism can be proposed accordingly to improve energy confinement for future EAST experiments. If we suppose that the ITG R/L_{Ti} can be increased (e.g. by enhanced ion heating), the anomalous thermal transport induced by the TEM turbulence can be effectively suppressed and energy confinement can be improved accordingly, which will in turn lead to an even larger value of R/L_{Ti}. Note that this mechanism works more efficiently when R/L_{Ti} is below the critical value $R/L_{\mathrm{Ti}} = 11$, where a substantial improvement in energy confinement could be obtained with a moderate increment of ion heating power. Above the critical value, the thermal transport induced by ITG turbulence dominates and does not decrease with R/L_{Ti} anymore. Therefore, the critical value plays a crucial role in determining the value of R/L_{Ti} for a given ion heating power, and any approach that can upshift this critical value is beneficial to confinement improvement through this mechanism.

We now show that this improvement mechanism is valid for a wide range of parameters in such experiments. To illustrate this, a 2D contour plot of the growth rate dependence on R/L_{Ti} and R/L_{Te} is shown in figure 7 for the mode with $k_\theta \rho_s = 0.93$. The dashed line indicates the transition boundary between two types of instabilities of TEM and ITG. It can be seen that TEM can be efficiently stabilized by increasing R/L_{Ti} for any value of R/L_{Te} considered here. Also, the favorable region with lower growth rates is generally aligned with the transition boundary (essentially, the balance between electron heating and ion heating). Moreover, it is also interesting to note the distinct difference in the orientation of the contour lines between the two regions. In the TEM regime, R/L_{Te} has the same tendency as R/L_{Ti} along the contour line, which indicates that electron (ion) heating is beneficial to the improvement of ion (electron) confinement for a given heat diffusivity evaluated by quasilinear theory. In the ITG regime, however, contour lines in the longitudinal direction are observed, which imply it is likely to increase R/L_{Te} with enhanced electron heating power but hard to increase R/L_{Ti} with it. Specifically, in this regime, the ITG tends to 'clamp', even with strong electron heating, which may be relevant to the recent experimental observations on AUG and W7-X [30].

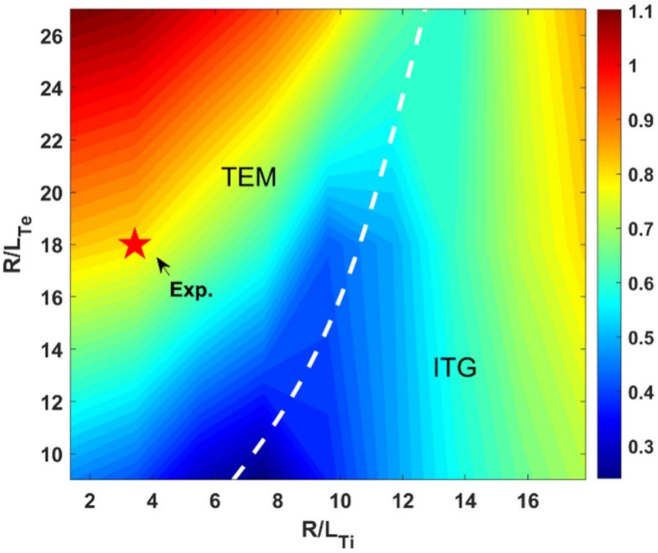

Figure 7. A parameter scan of the normalized growth rate and corresponding dominant instability for two drive forces of (R/L_{Te}, R/L_{Ti}). The normalized poloidal wavenumber is taken as $k_\theta \rho_s = 0.93$. The color bar means the values of the growth rate. The dashed arc indicates the transition boundary between TEM and ITG, and the pentagram indicates the experimental value.

The linear growth rates and frequencies for the microinstabilities computed with and without fast ions are compared in figure 9. It can be seen that fast ions also have few impacts on the growth rate and frequency for TEM, even when combined with the electromagnetic effects. Recent gyrokinetic simulations for high β plasma on JT-60U have also shown that the steep fast-ion pressure profile brought by the neutral beam injection seems to barely affect the TEM-induced turbulent transport, in both linear and nonlinear conditions [32]. It is found that unlike the fact that fast ions could reduce the ITG-induced turbulent transport, the significant fast-ion population have a different role in TEM-dominated systems [32].

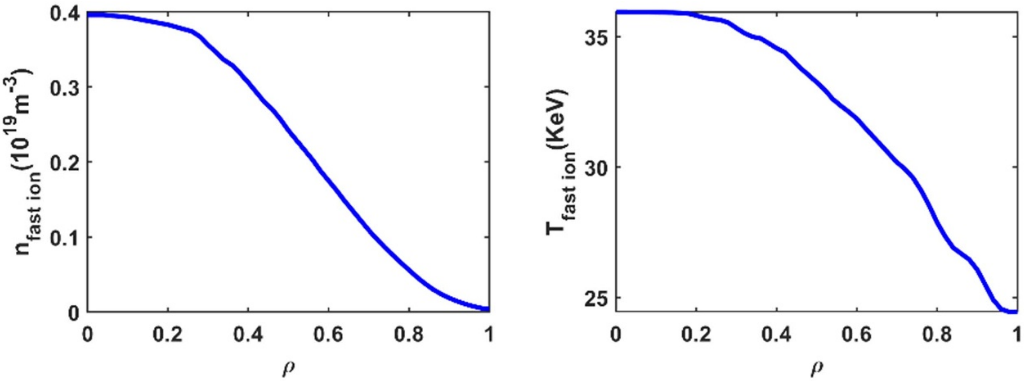

Figure 8. The density and effective temperature profiles of fast ions obtained by the TGCO code.

3.2. The effects of fast-ion and electromagnetic effects on TEM

To verify the effects of fast ions and electromagnetic perturbations on the stability of the dominant micro-instability in EAST core plasmas, we have performed the following simulations. The fast-ion profiles are calculated using the TGCO code [31], which is a guiding center Monte-Carlo simulation code for neutral beam ionization and collision transport of the injected beam ions. The density and effective temperature profiles of fast ions are shown in figure 8. It can be seen that the density of the fast ions is relatively low, which is partially due to the substantial fraction of shine-through and first orbit lost. The volume-averaged pressure of fast ions is 19.2% of the total pressure.

Electromagnetic simulations have also been carried out using NLT with the re-splitting scheme [33], which is effective for mitigating the cancellation problem in the gyrokinetic simulation with $p_{||}$ formulation. This algorithm has recently been implemented in the NLT code to include the shear Alfvénic perturbations ($\delta A_{||}$) for global simulation. It can be seen in figure 9 that the electromagnetic effects on the stability of TEM are rather small and can be ignored for EAST high-β_p plasma. This is reasonable since similar results of the negligible finite-β effects on the TEM mode have also been reported in [34] by the GYRO code and [35] by the GKV code. Taking the above simulation results and analysis into consideration, electrostatic simulations are carried out in this work and the effects of fast ions are neglected.

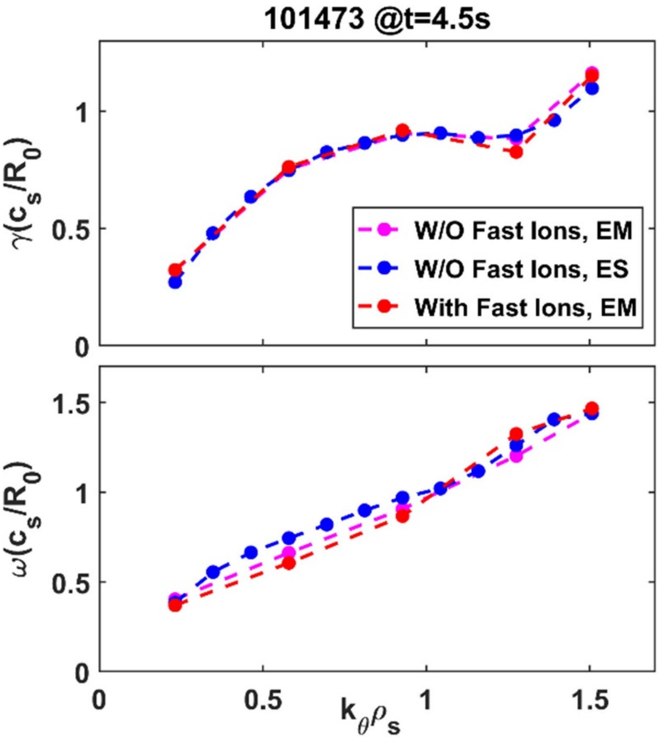

Figure 9. The growth rate and frequency of TEM with fast ions and electromagnetic perturbations. It can be found that the effects of fast ions and magnetic perturbation are small for TEM in this discharge.

3.3. Critical gradient threshold analysis

In this subsection, the radial distribution of the micro-instabilities is analyzed using the critical gradient threshold method. The critical gradient for TEM has been derived in the limit of a circular plasma [36] as

$$R/L_{T_{\text{ecrit}}} = \frac{0.357\sqrt{\varepsilon}+0.271}{\sqrt{\varepsilon}} \times \left[4.9-1.31\frac{R}{L_n}+2.68\hat{s}+\ln\left(1+20\nu_{\text{eff}}\right)\right]. \quad (1)$$

Here, $\hat{s}=(r/q)\,\partial q/\partial r$ is the magnetic shear, and the effective collisionality is $\nu_{\text{eff}}=\nu_{\text{ei}}/\omega_{\text{de}}\approx 0.1 n_e\left[10^{19}\right]Z_{\text{eff}}R\,[m]/T^2\left[keV^2\right]$.

The ITG threshold with multi-ion species is given by [37, 38] as

$$R/L_{T_{\text{icrit}}} = f\cdot g\cdot h \quad (2)$$

where

$$f = 1-\frac{0.2Z_{\text{eff}}^2}{s^{0.7}}\left(\frac{14\varepsilon^{1.3}}{\nu^{0.2}}-1\right) \quad (3)$$

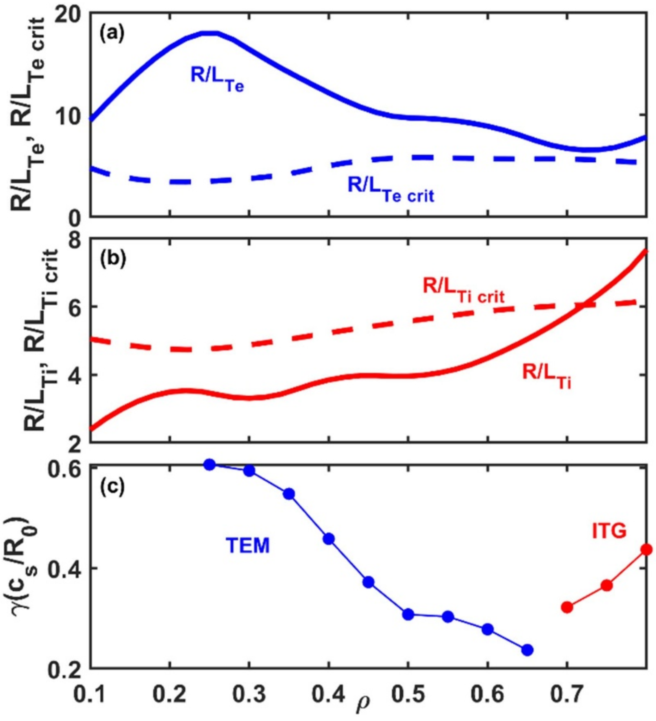

Figure 10. (a) $R/L_{\rm Te}$ and the calculated normalized linear TEM critical electron temperature gradient $R/L_{\rm Te\ crit}$; (b) $R/L_{\rm Ti}$ and $R/L_{\rm Ti\ crit}$; (c) the profile of growth rate with mode at $k_\theta\rho_s = 0.46$, where ITG exists.

$$g=\left(0.7+0.6s-0.2\frac{R}{L_n^*}\right)^2+0.4+0.3\left(\frac{R}{L_n^*}-0.8s+0.2s^2\right) \tag{4}$$

and

$$h=1.5\left(1+\frac{2.8}{q^2}\right)^{0.26}(Z_{\rm eff})^{0.7}\left(\frac{T_{\rm i}}{T_{\rm e}}\right)^{0.5} \tag{5}$$

with $\nu = 2.1Rn_e\left[10^{19}\right]/\left(T_{\rm e}^{1.5}T_{\rm i}^{0.5}\right)$ and $R/L_n^* = \max\left(6,\ R/L_n\right)$.

As shown in figure 10, the experimental profiles of $R/L_{\rm Te}$ and $R/L_{\rm Ti}$ are plotted and compared with the profiles of the critical gradient threshold calculated from equations (1) and (2). It can be seen in figure 10(a) that $R/L_{\rm Te}$ is far beyond the TEM critical gradient in the core region ($0.1 < \rho < 0.5$) while, for $\rho > 0.5$, the experimental $R/L_{\rm Te}$ gets close to the TEM critical gradient, indicating the relatively weak driving of TEM instabilities there. For $\rho > 0.6$, $R/L_{\rm Ti}$ increases with ρ rapidly and exceeds the ITG threshold. One can thus find from the critical gradient threshold analysis above that in such an experimental scenario with dominant electron heating, TEM dominates in the core region ($\rho < 0.5$), while ITG can play an important role in the outer region ($\rho > 0.6$). This result can also be confirmed by gyrokinetic simulation. In figure 10(c), linear simulations with a fixed wave number $k_\theta\rho_s = 0.46$ are carried out for a set of different radial positions. It is clear that the mode transforms from TEM to ITG as ρ increases from 0.2 to 0.8, which is generally consistent with threshold analysis. Therefore, TEM dominates the low-k turbulence in the core region ($\rho < 0.5$), where the electron thermal ITB is formed.

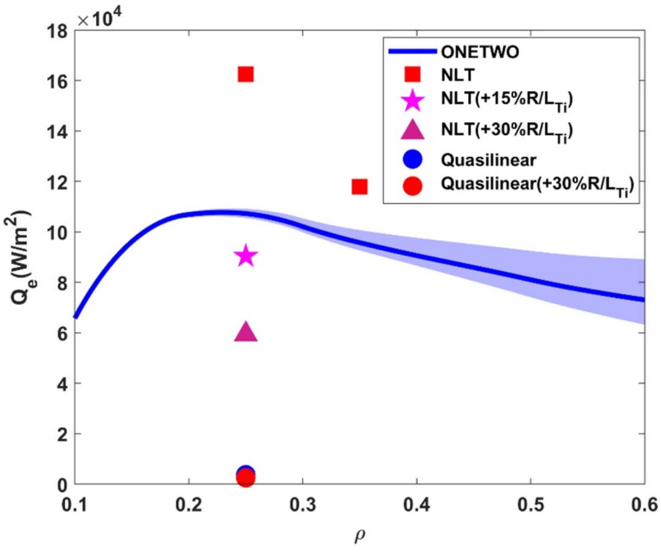

Figure 11. Energy fluxes of electrons: the solid line is simulated by ONETWO, the red squares are simulated by NLT, and the pentagram and triangle mean the energy fluxes with the experimental profile gradient $R/L_{\rm Ti}$ increased by 15% and 30%, respectively. The circles mean energy fluxes with the experimental $R/L_{\rm Ti}$ (blue) and 30% increased $R/L_{\rm Ti}$ (red) given by quasilinear calculation.

4. Nonlinear turbulence simulation and thermal transport analysis

Nonlinear gyrokinetic simulations are also carried out to quantitatively investigate the anomalous energy flux induced by core turbulence. The study mainly focuses on the electron thermal transport since the energy of electrons dominates over that of ions in this scenario. The simulations include 32 toroidal modes in total, corresponding to $0 \leqslant k_\theta\rho_s \leqslant 2.23$, in the 1/3 wedge of the full torus with the periodic boundary conditions in the toroidal direction. The time step is set as $t = 5\omega_{\rm ci}$, with a time diffusion coefficient $\nu = 0.01/\omega_{\rm DW}$ to mitigate the numerical instabilities induced by the high-frequency electrostatic Alfvén wave [22], where $\omega_{\rm ci}$ is the ion gyro-frequency and $\omega_{\rm DW}$ is the linear frequency of the drift wave. The size of the radial simulation box in the local simulation is $0.3a$ centered at the selected radial position, and the number of radial simulation grids $n_x = 256$. Two local simulations are firstly carried out at $\rho = 0.25$ and $\rho = 0.35$, respectively. In figure 11, the electron turbulent energy fluxes from NLT (the red squares) simulation are compared with experimental results given by power balance analysis (the blue line). It can be seen that good agreement between the two codes can be obtained for the values of the electron energy flux and the variation tendency from two codes in the core region. The nonlinear gyrokinetic simulations confirm that strong energy flux can be induced by TEM turbulence in the core of the plasma. The electron energy flux calculated by the NLT is 1.52 times that of ONETWO at $\rho = 0.25$, and 1.07 times at $\rho = 0.33$. The

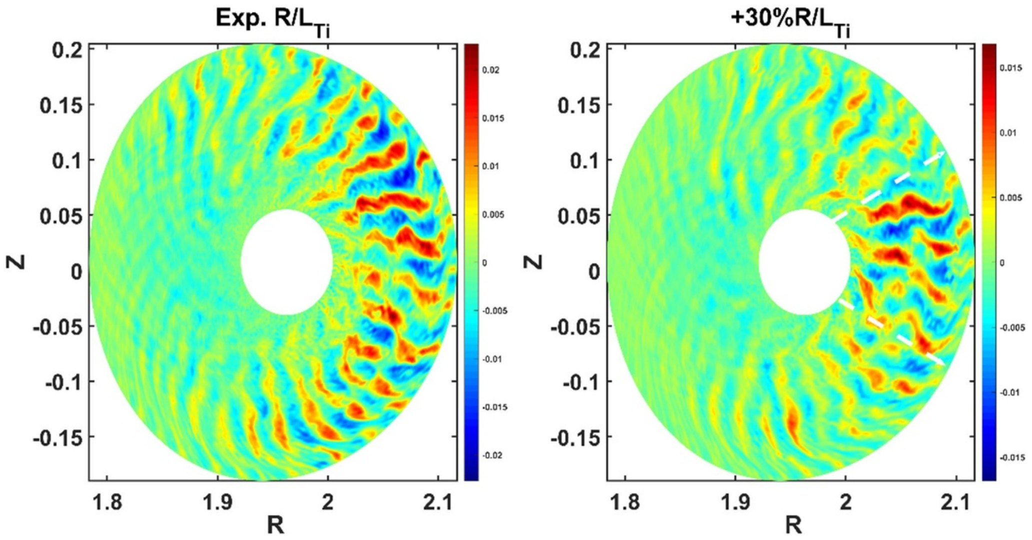

Figure 12. The turbulence structure with the experimental R/L_{Ti} and improved 30% R/L_{Ti}, respectively.

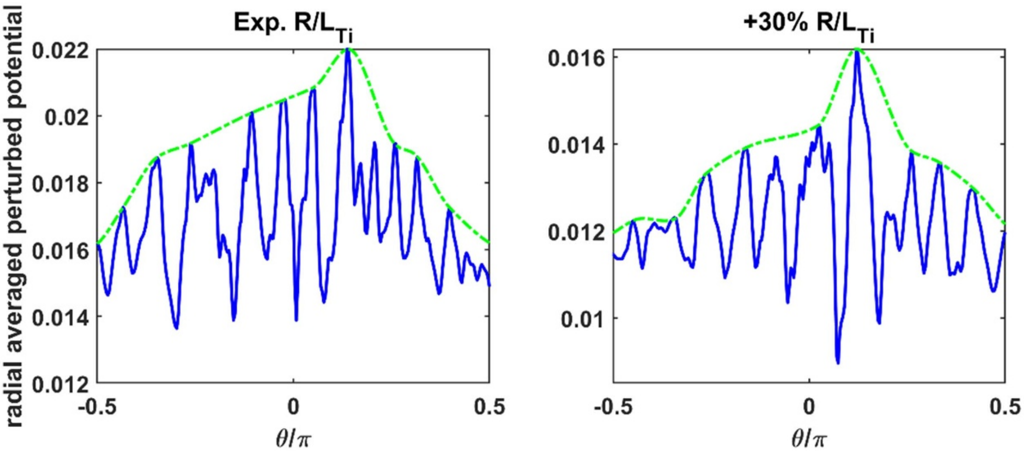

Figure 13. The radial-averaged perturbed potential as a function of the poloidal angle, for the experimental R/L_{Ti} and 30% increased R/L_{Ti}, respectively.

discrepancy at $\rho = 0.25$ may be attributed to the uncertainty in experimental measurements, such as the ion temperature profile. To illustrate this, another two simulations are performed with an artificially increased value of R/L_{Ti}. The pentagram and triangle symbols in figure 11 indicate that the energy fluxes with the experimental profile gradient R/L_{Ti} increased by 15% and 30%, respectively. The energy flux drops heavily with increased ITG; a 15% increment of R/L_{Ti} can give rise to about a 40% decrease in electron energy flux with the original R/L_{Ti}. The observed turbulence mitigation here is qualitatively consistent with the linear analysis of the growth rate reduction by R/L_{Ti} discussed in section 3.1. The quasilinear heat flux is calculated according to [39] and compared with the nonlinear results, and are shown in figure 11. The energy fluxes decrease by 32.5% with a 30% increment of R/L_{Ti} based on the quasilinear calculation, while the energy fluxes decrease by 63.4% from nonlinear gyrokinetic simulation. We find that the suppression effects evaluated by the quasilinear calculations are much lower than that of the nonlinear simulation, which implies the potential nonlinear suppression mechanism of TEM turbulence through increasing ITG. Nevertheless, both the linear and the nonlinear simulations confirm the validity of the confinement improvement through enhanced ion heating for relevant experiments.

To investigate the nonlinear mechanism of turbulence mitigation with increasing R/L_{Ti}, the structures of turbulence eddies are compared for the two cases at the same time, which is shown in figure 12. It can be observed that the size of the turbulence eddies is comparable around the low-field side ($0 < |\theta| < \pi/3$). This is reasonable since TEM is mainly driven by the trapped electrons, which are distributed mostly in the low-field region. However, with an artificially higher value of R/L_{Ti}, the mode structure becomes more ballooned. Specifically, the turbulence eddies with higher R/L_{Ti} become much weaker in amplitude and smaller in size for $\pi/3 < |\theta| < \pi/2$ in comparison with those with the nominal value of R/L_{Ti}. To further verify this, the poloidal structures of the radial-averaged perturbed potential are calculated and plotted in figure 13. It

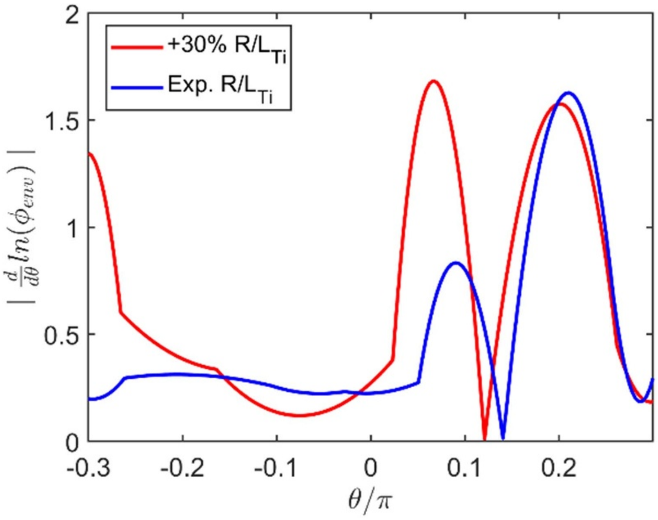

Figure 14. The poloidal gradient of the envelope of the radial-averaged perturbed potential.

can be seen that the increased R/L_{Ti} can induce an enhanced falloff of the perturbed potential as the poloidal angle moves away from the bad curvature region. To quantitatively compare the declined degree of the perturbed potential, we take the envelopes of the radial-averaged perturbed potential, which are indicated by the green lines shown in figure 13. As shown in figure 14, the poloidal gradient of the envelope of the radial-averaged perturbed potential with 30% increased R/L_{Ti} is generally larger than that with the experimental R/L_{Ti}, especially near the bad curvature region. Therefore, the surface-averaged turbulence flux can be decreased accordingly.

To interpret the transport properties in the EAST high-β_{P} experiment, the global turbulence simulation is also carried out in the ITB region. Compared with the local simulation, the radial size of the simulation box ($0.1 < \rho < 0.55$) is larger and the number of radial grid points is increased to 512 accordingly. As shown in figure 15, the profile of the electron turbulent thermal diffusivity calculated by NLT (red) in the ITB region is compared with electron thermal diffusivity given by power balance analysis (blue). The turbulence-induced effective thermal diffusivity shows good agreement with the measured diffusivity. The electron turbulent thermal diffusivity decreases obviously from the outer region to the core region in the area $0.2 < \rho < 0.5$, which accounts for the turbulent transport reduction in the ITB region contributing to confinement improvement. Therefore, one can conclude from this observation that the formation of e-ITB in the EAST high-β_{P} experiment is determined by the TEM-induced turbulence transport.

We next further investigate the potential mechanism of the e-ITB formation. The profile of the zonal flow shearing rate is calculated and shown in figure 16. The $E \times B$ shearing rate is defined by [40] $\omega_{E\times B} = \frac{r}{q}\frac{\partial}{\partial r}\left(\frac{q v_{E\times B}}{r}\right) \approx \frac{r}{q}\frac{\partial}{\partial r}\left(\frac{qE_{\mathrm{r}}}{rB}\right)$, where E_{r} is the radial electric field. Clearly, a much higher zonal flow shearing rate can be observed in the inner region ($0.2 < \rho < 0.34$), which could regulate energy transport induced by TEM turbulence efficiently and facilitate the formation of e-ITB.

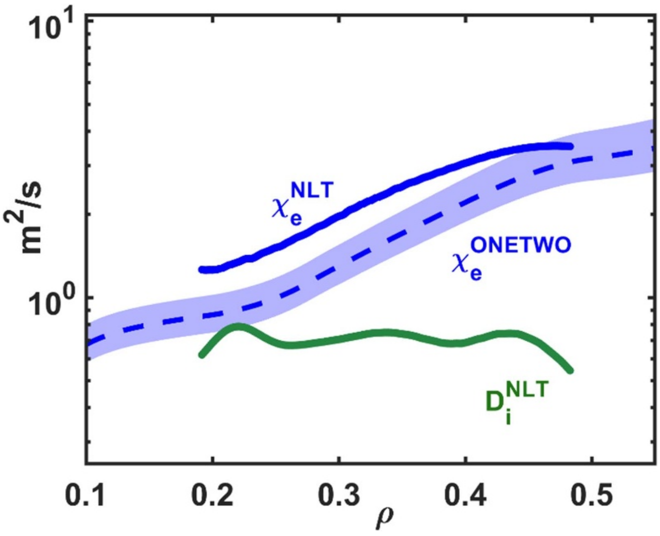

Figure 15. Electron (blue) thermal diffusivities given by NLT and ONETWO, and the ion diffusivity given by NLT (green).

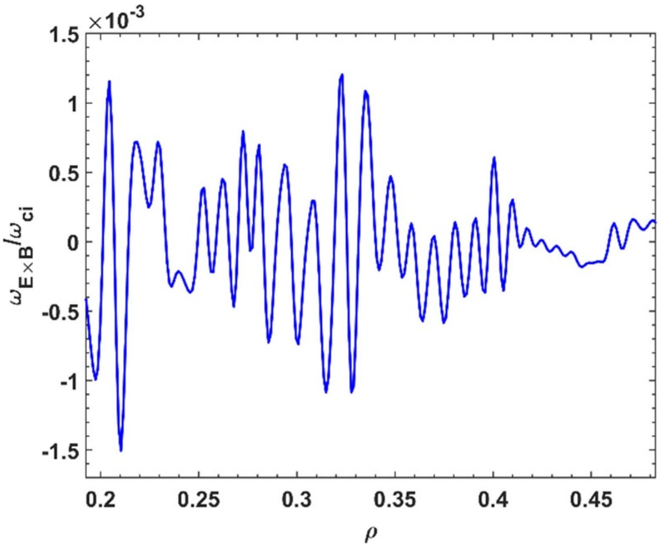

Figure 16. The zonal shearing rate profiles at 4.5 s for #101473.

5. Conclusions

Core turbulence and thermal transport are studied for EAST high-β_{P} plasma. The analysis of the growth rate and frequency of the most unstable modes spectrum shows that TEM is the dominant instability in ion-scale perturbations. Both the linear properties and the suppression mechanism of the unstable mode are systematically investigated via gyrokinetic simulations. The numerical results show that the TEM instability could be stabilized by increasing R/L_{Ti} but destabilized by increasing R/L_{Te}. A positive feedback mechanism for confinement improvement is proposed by increasing R/L_{Ti}. As R/L_{Ti}

increases, the transition from TEM to ITG is observed. When $R/L_{\mathrm{ne}} < 4$, TEM is destabilized; however, when $R/L_{\mathrm{ne}} > 4$, the increased R/L_{ne} can stabilize both the TEM and ITG. It is found that at the experimental value of R/L_{Te}, a doubled R/L_{Ti} could significantly reduce the TEM turbulence growth rate to half of its original value. The simulation results also indicate that increasing R/L_{Te} would destabilize the TEM as well as the ITG. When comparing the dominant turbulence in the low-k range together with the gradient threshold, one finds that when R/L_{Te} is significantly larger than the critical threshold gradient, the TEM growth rate is large and the thermal transport of both electrons and ions increases until R/L_{Te} approaches the threshold. As R/L_{Ti} increases, the dominant low-k instabilities turn to ITG mode.

The nonlinear gyrokinetic simulations given by NLT have been quantitatively compared with the experimental values calculated by ONETWO, which confirms that the electron energy flux measured in the experiment in the core region is induced by TEM turbulence. The zonal flow shearing rate is found to be higher in the ITB region, which could regulate energy transport induced by TEM turbulence efficiently and facilitate the formation of e-ITB. The effects of the scale length of the ITG on the electron turbulent energy flux have also been identified via the nonlinear simulation to be the suppression of the turbulent eddy size and amplitude in the region away from the bad curvature region. Therefore, the enhancement of ion heating to mitigate turbulence transport and improve confinement is proposed for future experiments. Moreover, to actively improve the confinement in high-β_{P} discharge, the suppression effect of Shafranov shift and negative magnetic shear on turbulent transport will also be investigated further in future work [21].

Data availability statement

The data that support the findings of this study are available upon reasonable request from the authors.

Acknowledgments

The authors would like to thank Professor Shaojie Wang and Dr Debing Zhang for helpful discussions. This work is supported by the National MCF Energy R&D Program (2019YFE03040000 and 2022YFE03050000), the National Natural Science Foundation of China under Contract Nos. 12005262 and 11975274, the US Department of Energy, Office of Science, Office of Fusion Energy Sciences Cooperative Agreements DE-FC02-04ER54698 and DE-SC0010685, the Collaborative Innovation Program of Hefei Science Center, CAS under Grant 2022HSC-CIP008, the Anhui Provincial Natural Science Foundation No. 2108085J06, the Users with Excellence Program of Hefei Science Center CAS under Grant Nos. 2021HSC-UE018 and 2020HSC-UE011 and the Science Foundation of the Institute of Plasma Physics, Chinese Academy of Sciences, No. DSJJ-2021-04. Part of the numerical computations were performed on ShenMa High Performance Computing Cluster at the Institute of Plasma Physics, Chinese Academy of Science, National Supercomputer Center in Tianjin and Hefei Advanced Computing Center.

ORCID iDs

Y C Hu https://orcid.org/0000-0001-5791-9374
L Ye https://orcid.org/0000-0002-6505-6625
A M Garofalo https://orcid.org/0000-0002-8244-2448
B Zhang https://orcid.org/0000-0003-0304-2372
Y J Hu https://orcid.org/0000-0002-6764-5538
X X Zhang https://orcid.org/0000-0002-3596-9212

References

[1] Hayashi N 2017 *Nucl. Fusion* **57** 126037
[2] McClenaghan J 2019 *Nucl. Fusion* **59** 124002
[3] Jian X 2019 *Phys. Rev. Lett.* **123** 225002
[4] Ding S 2017 *Phys. Plasmas* **24** 056114
[5] Kamada Y 2002 *Fusion Sci. Technol.* **42** 185–254
[6] Thomas P R 1994 *Plasma Phys. Control. Fusion* **36** B301
[7] Pan C 2017 *Nucl. Fusion* **57** 036018
[8] Staebler G M 2018 *Phys. Plasmas* **25** 056113
[9] Staebler G M 2018 *Nucl. Fusion* **58** 115001
[10] Ding S 2020 *Nucl. Fusion* **60** 016023
[11] Gong X 2019 *Nucl. Fusion* **59** 086030
[12] Gong X 2022 *Nucl. Fusion* **62** 076009
[13] Ye L 2016 *J. Comput. Phys.* **316** 180–92
[14] Wu M Q 2019 *Nucl. Fusion* **59** 106009
[15] Qian J P 2021 *Phys. Plasmas* **28** 042506
[16] Lao L L 1990 *Nucl. Fusion* **30** 1035–49
[17] Liu H Q 2016 *Rev. Sci. Instrum.* **87** 11D903
[18] Qian J P 2017 *Nucl. Fusion* **57** 056008
[19] Wang S 2012 *Phys. Plasmas* **19** 062504
[20] Wang S 2013 *Phys. Plasmas* **20** 082312
[21] Wang S 2014 *Phys. Plasmas* **21** 023509
[22] Zhao P F 2021 *Comput. Phys. Commun.* **269** 108114
[23] Chen Y 2015 *Rev. Sci. Instrum.* **86** 023509
[24] Weiland J 1989 *Nucl. Fusion* **29** 1810–4
[25] Coppi B 1977 *Nucl. Fusion* **17** 969–93
[26] Carralero D 2021 *Nucl. Fusion* **61** 096015
[27] Team E 2020 *Chin. Phys. Lett.* **37** 045202
[28] Waltz R E 1994 *Phys. Plasmas* **1** 2229–44
[29] Kim J Y 2017 *Phys. Plasmas* **24** 072501
[30] Beurskens M N 2021 *Nucl. Fusion* **61** 116072
[31] Hu Y 2021 *Phys. Plasmas* **28** 112105
[32] Mazzi S 2020 *Nucl. Fusion* **60** 046026
[33] Ye L 2020 *Comput. Phys. Commun.* **250** 107050
[34] Belli E A 2010 *Phys. Plasmas* **17** 112314
[35] Ishizawa A 2015 *J. Plasma Phys.* **81** 0–47
[36] Peeters A G 2005 *Phys. Plasmas* **12** 022505
[37] Kotschenreuther M 1995 *Phys. Plasmas* **2** 2381–9
[38] Erba M 1999 *Nucl. Fusion* **39** 495–507
[39] Adam J C 1976 *Phys. Fluids* **19** 561–6
[40] Waltz R E 1998 *Phys. Plasmas* **5** 1784–92